Additive Manufacturing 37 (2021) 101649

Contents lists available at ScienceDirect

Additive Manufacturing

journal homepage: www.elsevier.com/locate/addma

Research Paper

Improved grain structure prediction in metal additive manufacturing using a Dynamic Kinetic Monte Carlo framework

Sumair Sunny [1,2], Haoliang Yu [1,2], Ritin Mathews [2], Arif Malik [*,2], Wei Li [2]

Department of Mechanical Engineering, The University of Texas at Dallas, Richardson, TX 75080, USA

ARTICLE INFO

Keywords:
Selective laser melting
Powder bed fusion
Additive manufacturing
Grain structure prediction
Dynamic Kinetic Monte Carlo
Numerical modeling
Electron backscatter diffraction

ABSTRACT

This work describes a Dynamic Kinetic Monte Carlo numerical modeling framework that can predict the microstructure of metals during powder bed fusion (PBF) and directed energy deposition (DED) additive manufacturing (AM) while considering significant variations in thermal history and heat accumulation that occur during the build. Although the conventional Kinetic Monte Carlo (KMC) method is well-established, it does not accommodate variation in the spatial domains of the melt pool (MP) and heat affected zone (HAZ) with time. Thus, the predicted microstructure remains relatively similar even over large AM build domains. While the existing KMC approach may suffice over spatial regions in which the MP and HAZ remain relatively unchanged, this circumstance is largely contrary to what experimentalists have recently found when imaging different regions in PBF and DED AM builds, thus raising issues with scalability and versatility of the method. The Dynamic KMC framework proposed in this work addresses these concerns by implementing discretized, spatially-varying MP and HAZ at every time increment during the grain structure prediction. The new framework operates in two stages; stage one establishes the 3D spatial MP and HAZ dimensions using either thermal finite element (FE) simulation or through experimental 3D thermal imaging; stage two subsequently integrates these time-varying MP and HAZ dimensions into the KMC algorithm at every time increment during the build. Thus, the Dynamic KMC framework captures the effects that rapid thermal cycles and heat accumulation have on grain nucleation and growth. The method is demonstrated through a case study involving a thin-walled Inconel 625 structure made by the selective laser melting (SLM) type of laser-based powder bed fusion (PBF-LB). The numerically predicted microstructures at various regions and scan layers within the build show strong agreement with experimentally observed trends reported in literature. Significant variations in grain morphology predicted by the Dynamic KMC framework can, according to specific thermal histories, provide investigators with new capabilities in assessing mechanical property variations across different regions of AM parts.

1. Introduction

Metal additive manufacturing methods are known to influence the size, shape, and orientation of grains, and therefore the mechanical as well as other properties that result [1,2]. The relatively recent emergence of commercial applications involving metal AM products necessarily demands more iterative cycles for prototype design, fabrication, and testing compared to conventional manufacturing processes. Since such trial and error is time consuming and expensive, competitive growth in the application of metal AM parts will benefit from improved modeling and prediction tools. Hence, both numerical predictions and experimental observations that elucidate the effects of varying AM process parameters on grain morphology are of great interest to current metal AM research.

1.1. Recent experimental observations of metal AM grain structure

Discussed next are some recent experimental observations that are relevant to both the proposed Dynamic KMC prediction capability as well as to the findings in the case study examined later in this paper.

* Corresponding author.
E-mail address: Arif.Malik@utdallas.edu (A. Malik).
[1] Joint first author
[2] ORCID(s): 0000-0003-3678-9368 (S. Sunny); 0000-0003-3558-669X (H. Yu); 0000-0003-0144-0828 (R. Mathews);0000-0002-2043-5568 (A. Malik); 0000-0002-0653-5300 (W. Li).

https://doi.org/10.1016/j.addma.2020.101649
Received 4 April 2020; Received in revised form 23 August 2020; Accepted 5 October 2020
Available online 13 October 2020

In 2014, Carter et al. [3] used scanning electron microscopy (SEM) and electron backscatter diffraction (EBSD) imaging to study the effects of laser scan strategy on grain structure in the selective laser melting (SLM) of nickel superalloy (CM247LC). They observed a mix of elongated (columnar) and spherical (equiaxed) grains along the build direction. The variation in the grain shape observed was associated to the rate of cooling and the direction of heat flow. They deduced that, depending on the amount of overlap in scans, it is better to consider the laser induced heat source as a band rather than as a point source. They further noted that the presence of columnar and equiaxed grains may be undesirable since "weak points," prone to cracking, can arise in the microstructure due to high misorientation of grain boundaries.

In 2016, Wang et al. [4] used EBSD imaging to quantitatively describe the grain structure seen at two different sections along the build direction of a 304L thin-walled DED structure (110 mm long × 11 mm wide × 70 mm tall). As seen in Fig. 1a, an image of a section taken 15 mm from the top of the wall reveals an inhomogeneous microstructure with grains largely approaching an equiaxed morphology. In contrast, Fig. 1b taken from a section 7 mm from the bottom of the wall reveals a microstructure consisting of columnar grains that tend to grow in the direction of maximum thermal gradient as successive layers are deposited.

In 2017, Sun et al. [5] parametrically examined the effects of laser power, scan speed, and scan strategy on SLM fabricated 316 L stainless steel specimens. They found that using perpendicularly varying scan orientations in consecutive layers helped mitigate the presence of pores due to lack of fusion between the successive layers. Moreover, their EBSD results revealed the presence and distribution of elongated and equiaxed grains, seen in Fig. 1c. Finer, more equiaxed grains were seen at the bottom of the build as well as near the top layer, with elongated grains forming in the middle layers. From their work, it can be concluded that the HAZ of a currently scanned layer can cause grain growth in layers directly beneath it.

In 2019, Holland et al. [6] investigated the microstructures formed at different locations along the build direction of a SLM fabricated Inconel 718 specimen. Optical microscopy revealed elongated (or columnar) grain formation aligning along regions coincident with high temperature gradients. The specimens were also heat treated, and the accumulation of residual thermal stress from repeated thermal cycles was found to give rise to the formation of homogenized as well as annealing twin grain structures. As noted by Wang et al. [4], with regard to location, the top and middle sections in the SLM build direction exhibit columnar grains with equiaxed grains forming near the solidification front. This pattern is associated to the rapid cooling observed in SLM; grain structures at the bottom exhibit less of a distinct pattern and relatively greater randomness. Such variation in grain structure along the build direction is attributed to the transient thermal history inherent to the SLM manufacturing process. The observations of Wang et al. showed some agreement with the EBSD images documented in the work of Fang et al., as seen in Fig. 1d [1].

The experimental observations in the aforementioned studies indicate variations in grain structures that can be attributed to growth of the melt pool (MP) and heat affected zone (HAZ) resulting from non-uniform heat accumulation during the particular AM builds. Note that the experimental imaging techniques used in these studies (and those involving conventional manufacturing processes) typically produce characterization data (and generate insights) for very small regions of parts; thus, a large number of such characterizations are needed to analyze and comprehensively assess grain structures over large and/or geometrically distinct regions, including at different build depths in AM processes. Accordingly, various computational modeling approaches to predict grain structure have been pursued over the past few decades. A summary of the computational grain prediction methods used for metal AM is provided in the following section, with the majority of the discussion focused on Kinetic Monte Carlo since it provides the foundation for the Dynamic KMC framework introduced and demonstrated in this work.

1.2. Overview of numerical prediction of metal AM grain structure

In 2001, Holm and Battaile [7] discussed the use of various methods to predict grain structure, including Cellular Automata (CA), Phase Field

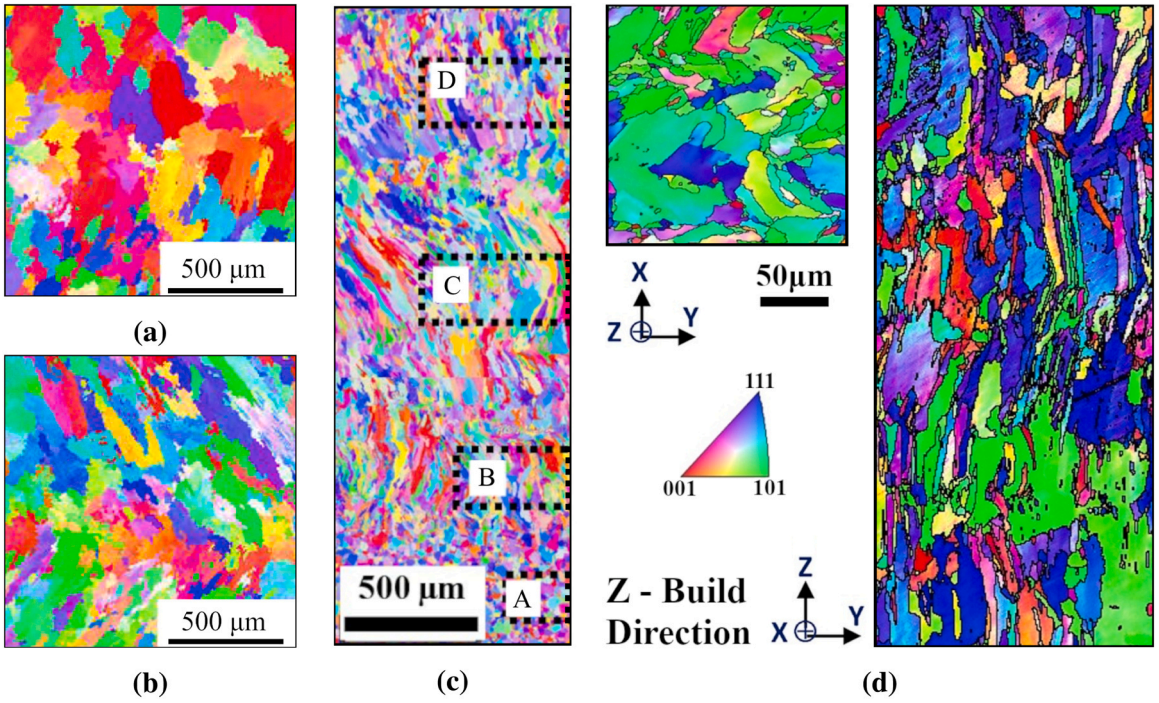

Fig. 1. (a) EBSD images adapted from Wang et al. [4] featuring inhomogenous grain structures, 15 mm from the top of the wall, and (b) 7 mm from the bottom of the wall. (c) EBSD image adapted from Sun et al. [5] showing grain structure variation along the build direction. (d) EBSD images adapted from Fang et al. [1] showing grain structure variation along the build direction.

Modeling (PFM), and Kinetic Monte Carlo. Cellular Automata had primarily been applied in simulations of biological system development. Liu et al. [8], however, combined CA with a Monte Carlo statistical method to create a model to simulate grain nucleation and growth. Several researchers have since modified CA models to augment their capabilities, and CA can now be coupled with thermal simulations to numerically predict grain structures in 3D domains, incorporating the effects of grain orientation, material deformation, and dislocations [9,10]. Application of CA models has been extended to grain structure prediction in metal AM parts [11]. Recent developments in 3D CA simulations for AM microstructure prediction, as described by Lian et al., show qualitative agreement with the EBSD imaging reported in Antonysamy et al.'s work [12,13].

A multiscale framework utilizing PFM for microstructure prediction of AM metal alloys was discussed in 2018 by Ji et al. [14]. Thermal histories from a macroscopic scale FE model based on selective electron beam melting (SEBM) were used as input for the grain growth or solidification PFM. The results of Ji et al.'s framework with Ti6Al4V depict similar trends when compared to experimental observations by Antonysamy et al. [13,15]. Columnar grains were observed to form parallel to the build direction, with small grains near the section edges. The development of columnar grains was noted to induce anisotropic mechanical properties.

Prediction of metallic grain structures using Kinetic Monte Carlo has its origins with the Potts model [16], which was initially intended for magnetic domain discretization and evolution. Work by Anderson et al. [17] in the 1980s, however, illustrated the model's versatility towards grain structure prediction for polycrystalline materials given the similarities between grain structures and Potts domain structures. Over the next two decades, the Kinetic Monte Carlo Potts model (or simply KMC model) was refined to model grain growth, recrystallization, and solidification. Much later, in 2017, Rodgers et al. discussed a *modified* KMC model that enabled 3D modeling of grain structure evolution in AM processes. As discussed by Rodgers et al., peak temperature and temperature distributions were found to affect grain morphology in AM. Their work involved replicating electron beam melting (EBM), DED, and direct laser fabrication (DLF) experiments [13,18] using their modified KMC simulations. The results showed that a smaller, equiaxed grain structure prevailed along the scan path whilst columnar grains formed in the HAZ region between two successive scan paths [19]. This result explains how and why material properties of AM parts become anisotropic.

The fundamental workings of the Potts model, while not discussed here, can be found in [19]. In terms of KMC modifications specific to AM, the melt pool (MP) and heat affected zone (HAZ) were modeled similar to Goldak et al.'s 1984 double ellipsoid heat source [20], but simplifications rendered the size of both the MP and HAZ constant in the modified KMC model. Note, however, that with Goldak et al.'s model the input heat flux and material specific response can be used to determine time-varying dimensions of the MP and HAZ, and thus they need not be assumed constant. Indeed, as is illustrated later in Section 4, intralayer heat accumulation readily occurs in AM processes such as SLM, and the layer-specific thermal history can give rise to significant changes in the MP and HAZ boundaries. This is especially true when printing relatively small or thin-walled structures having short scan paths at high scan speeds [21,22]. Such corresponding growth of the MP and HAZ is believed to significantly affect the alloy's grain size and aspect ratio, as particularly influenced by factors governing the thermal history, such as part geometry, scan speed, powder layer thickness, laser power, ambient conditions, etc. The multi-second dwell time from when a layer is scanned to when the successive powder layer is deposited by the recoater may not allow for sufficient cooling, and thus some residual heat from the last scanned layer may transfer to the newly deposited powder layer before scanning of the new layer commences. Hence, the assumption of constant MP and HAZ in Rodgers et al.'s modified KMC model limits its ability to account for such grain structure variations, like those seen in Figs. 1a to d, as reported by [4,5,1], respectively.

With regard to SLM, the aforementioned and other limitations of the current (modified) KMC model are as follows: (1) Considers steady-state MP and HAZ - thus modeled grain structures remain relatively similar in shape and pattern even over large AM build domains; (2) Does not account for MP and HAZ *edge effects*, defined as abrupt changes to the MP and HAZ boundaries near an edge of the build geometry where one scan line terminates and an adjacent one commences (leading to directional discontinuity in the MP and HAZ); (3) Involves high computational cost, limiting the simulation domain; (4) Does not accommodate multi-phase solidification; (5) Does not provide crystallographic orientations among grains; (6) Only predicts grain nucleation and growth, hence other models are needed to predict keyhole effects (i.e. cavity formation) [23,24], residual stresses, and distortion in printed parts.

Despite the aforementioned limitations of the modified KMC model, subsequent investigations have cited its value. For example, Yan et al. in 2018 mention Rodgers et al.'s KMC model for use in a comprehensive data-driven predictive modeling suite spanning from SLM process parameters to mechanical properties of metal AM parts [25,26]. Rodgers et al. applied their KMC model to generate 3D, synthetic, voxelized microstructure for a 304L stainless steel DED thin-walled cylindrical build [27]. Simulations were performed parametrically using four different scan speeds to investigate the effect on microstructure. The predicted microstructures were further mapped into a conformal FE mesh and an anisotropic crystal elasticity constitutive material model was adopted. Under relatively simple loading conditions, the microstructures' influence on mechanical response was studied. In a similar study by Rodgers et al. (2020), a crystal plasticity-finite element model was used, in place of the crystal elasticity model, to predict plastic deformation of the simulated AM microstructures [28]. Strength and plastic anisotropy variations were observed when drawing comparisons with conventional equiaxed microstructures. In 2019, Li and Soshi used Rodgers et al.'s modified KMC model (2017) to predict the effects that different scan speeds have on grain structure [2]. Comparing microstructures predicted at lower speeds (0.45 m min^{-1}) to higher speeds (1 m min^{-1}), they observed the former gave a relatively reduced number of larger, equiaxed grains along the scan track and fewer but larger, elongated grains between scan tracks. On the other hand, the latter gave a relatively greater number of equiaxed grains along the scan track and a greater number of elongated grains between scan tracks, albeit those grains were comparatively smaller overall. As seen in Fig. 2, they compared EBSD results reported by Rodgers et al. [19], for a 304L stainless steel sample fabricated by DED, with their simulated results using the same process parameters. Trends observed when comparing the distributions for grain aspect ratio in the experimental and simulation results showed reasonable agreement since both Yan et al. and Li et al. applied Rodgers et al.'s modified KMC model, however the transient thermal histories in the respective AM builds were not taken into account. Thus, also disregarded were the ensuing effects of thermal history on grain structure variations occurring over larger regions within a given layer, or across multiple layers of a printed structure.

1.3. Motivation for development of Dynamic KMC model

In view of the above discussion on grain structure prediction methods, and in particular the capabilities and limitations of the existing KMC model, it is hypothesized that KMC grain structure prediction can be improved by implementing a *Dynamic* KMC framework that incorporates time-varying MP and HAZ dimensions during the build. Such a framework is therefore introduced in this paper, and results of the method for SLM with Inconel 625 are presented and compared to corresponding experimental observations reported in literature, as well as to results generated by the existing (modified) KMC model that uses constant MP and HAZ dimensions. As discussed further in Section 2, the Dynamic KMC approach incorporates heat accumulation effects, with the goal of providing more realistic grain structure predictions. Either

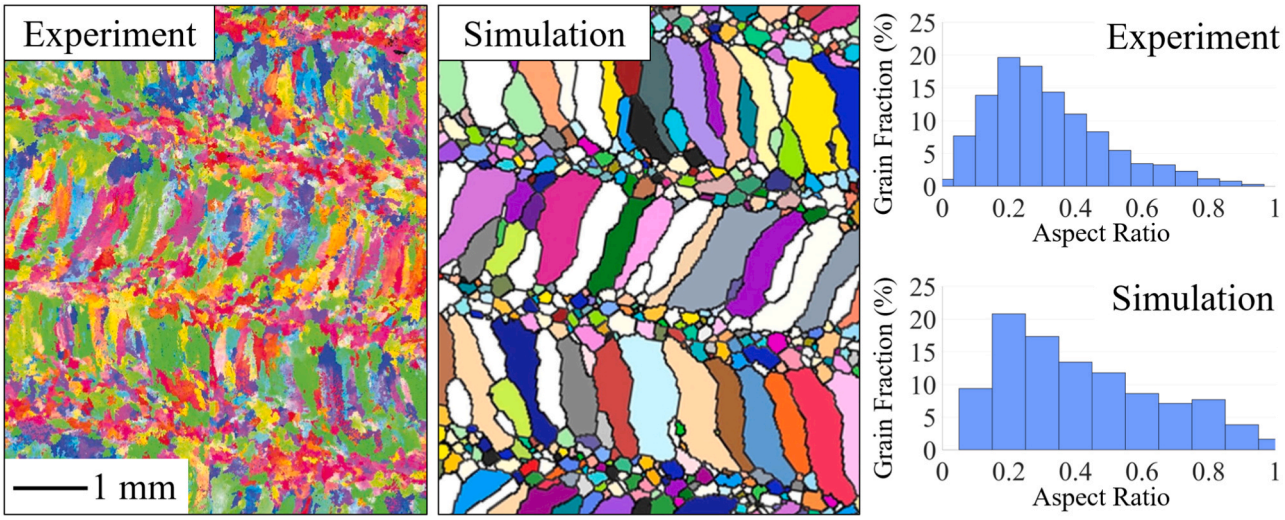

Fig. 2. Comparison of grain aspect ratio between an EBSD image of a 304L specimen made by DED, adapted from Rodgers et al. (2017) 19], and a KMC simulation considering the same process parameters adapted from Li and Soshi [2].

infrared (IR) imaging of the complete build process or a calibrated thermal simulation can be applied a priori to determine the time-varying MP and HAZ dimensions to be used by the Dynamic KMC model. In this work, a thermal FE model is incorporated, as described in Sections 3.1 and 3.2. Calibration of this FE model is performed using experimental IR data, as discussed in Section 3.3. The calibrated FE model is then applied with specific process parameters to predict the thermal history during SLM of IN625 powder to build a thin-walled structure (described in Section 3.4). A comparison of the resulting grain structure predictions using the proposed Dynamic KMC framework as well as the existing KMC model (with constant MP and HAZ dimensions) is presented and discussed in Section 4. Key observations and trends regarding evolution of the microstructure predicted by the Dynamic KMC framework are summarized in Section 5.

2. Dynamic KMC framework for metal AM grain morphology prediction

The basis of the KMC method is the Monte Carlo Potts model, an on-lattice technique developed for curvature driven grain growth. The underlying algorithm assigns an integer "spin" number to each lattice site, and neighboring sites that share the same spin number are assembled into one grain. Adjacent sites having different spin numbers contribute to the total system energy. Grain evolution is advanced by minimizing the system energy by way of performing Monte Carlo simulations (MCS) and re-assigning spin numbers for those sites on the grain boundary. To apply the KMC method to metal PBF and DED AM [29], Rodgers et al. specified two regions for use by the Monte Carlo Potts model, namely the MP and HAZ. Since grain growth is not expected significantly far away from the heat source (laser in SLM), and nucleation is only expected within the MP, the MCS are only performed for sites that fall within the HAZ, while the spin numbers are randomly assigned to all the sites within the MP. Additional details for the original Monte Carlo Potts model as well as the *modified* KMC model can be found in [7,19].

On the basis of Rodgers et al.'s work, the Dynamic KMC framework is established using a new algorithm shown in Fig. 3. The time-varying MP and HAZ dimensions are spatially defined during SLM as a function of temperature at each time increment, j. At the j^{th} increment, the hottest location (or Pool Origin) within the laser-scanned area (uppermost surface of deposited powder) is tracked and considered to be the epicenter of the laser. Isotherms in 3D space around this point provide information to determine the MP and HAZ boundaries at time increment j according to the respective melting and recrystallization temperatures of the material, T_m and T_R, per Eq. (1), where the MP and HAZ geometries are denoted MP_j and HAZ_j, respectively, for time increment j:

$$\left\{\begin{matrix}\text{MP}_j\\ \text{HAZ}_j\end{matrix}\right\} = \left\{\begin{matrix}\overline{\text{X}}, & \forall & T(\overline{\text{X}},t) \geq T_m & \text{for} & t = t_j\\ \overline{\text{X}}, & \forall & T_R < T(\overline{\text{X}},t) < T_m & \text{for} & t = t_j\end{matrix}\right\} \tag{1}$$

where $\overline{\text{X}}$ is the 3D coordinate location within the simulation domain for the material medium. As seen in Eq. (1), recrystallization temperature is used as the lower limit isotherm for the HAZ. This is based on a study of microstructure predictive modeling for an Inconel 718 DED process by Wei et al., who discuss how solid-state evolution in the Monte Carlo model is limited to regions within the HAZ boundary [30]. Repetitive cycles of re-heating and subsequent cooling in these regions result in changes to grain size. Regions of the fused continua at temperatures below the isotherm will exhibit no further changes in microstructure. Although their work does not explicitly mention any value for the isotherm, trial-and-error based calibration has been done in the present work using different case studies from the literature [1,5] that provide experimental SLM process parameters and accompanying EBSD images of the resulting microstructure. On that basis, recrystallization temperature is determined a suitable choice for the lower limit isotherm of the HAZ.

Once the 3D spatial geometries for MP_j and HAZ_j are identified, they are input to the dynamic KMC code as a spatial subset containing 8 time-dependent parameters λ_j (seen later in Fig. 8). These parameters are obtained by subtracting the distance between the Pool Origin and the respective isotherm boundaries delineating T_m and T_R along mutually orthogonal directions. Eq. (2) defines the $\boldsymbol{\lambda_j}$ set.

$$\boldsymbol{\lambda}_j = \left\{\begin{matrix}\text{MP} & \text{Width}\\ \text{MP} & \text{Tail}\\ \text{MP} & \text{Depth}\\ \text{MP} & \text{Cap}\\ \text{HAZ} & \text{Width}\\ \text{HAZ} & \text{Tail}\\ \text{HAZ} & \text{Depth}\\ \text{HAZ} & \text{Cap}\end{matrix}\right\}_j^{\top} \subset \left\{\begin{matrix}\text{MP}_j\\ \text{HAZ}_j\end{matrix}\right\}^{\top} \tag{2}$$

Before the λ_j are provided to the KMC code, conversion from physical dimensions to *sites* is required. Detailed discussion regarding the *sites* is provided in Section 4. Note that if the number of time increments '$\kappa_{\max}$' in the KMC simulation differs from that in the thermal simulation for '$j_{\max}$' (or no. of frames captured from a thermography experiment [31]), then linear interpolations for λ are performed to generate additional time increments between successive j increments while promoting smoother transitions. The culmination of the interpolation process is λ_κ,

which is simply a $\kappa_{max} \times 8$ matrix of parameters quantitatively expressed in terms of 'sites'. In the presented Dynamic KMC simulation, Rodgers et al.'s Potts model is internally revised to call the κ^{th} row of the matrix (λ_κ) as input for increment κ, thus realistically capturing the variation of MP and HAZ dimensions as predicted by thermal simulations or observed by thermography. Thus, the distinguishing feature of the Dynamic KMC framework is that it incorporates an updating algorithm for new MP and HAZ dimensions at each MCS time increment (κ). Note that while different sizes of the MP and HAZ can vary the computational cost, the Dynamic KMC framework itself does not introduce extra computational time. Since the matrix of parameters, λ_κ, defining the size and shape of the MP and HAZ over the entire PBF-AM process is known a priori, it will only be read once.

3. Numerical grain morphology study for SLM build

3.1. Finite element heat transfer model for SLM

Considering a PBF-LB process [29], the 3D spatial and temporal temperature field distribution for both the printed geometry and substrate powder is governed by Eq. (3).

$$\frac{\partial}{\partial x}\left(k\frac{\partial T}{\partial x}\right)+\frac{\partial}{\partial y}\left(k\frac{\partial T}{\partial y}\right)+\frac{\partial}{\partial z}\left(k\frac{\partial T}{\partial z}\right)+Q=c_p\rho\frac{\partial T}{\partial t},\quad \text{for}\quad t\geq 0 \tag{3}$$

which is applicable within the Lagrangian domain for temperature T (K) at time t (s). Term c_p (J kg^{-1} K^{-1}) is specific heat, ρ (kg m^{-3}) is density of the material, k (W m^{-1} K^{-1}) is thermal conductivity, and Q (W m^{-3}) denotes the volumetric heat input [32] induced by the laser. Properties differ for powder and solid continua, while both are temperature dependent [33–35]. The solid continua in the model includes the substrate and the volume of powder representing the thin-walled structure after melting and cooling. The powder continua's thermal conductivity is approximated to be 1% that of the solid continua, per Foroozmehr et al. [36]. Temperature-dependent thermal conductivity curves of IN625 in both powder and solid form have been sourced, respectively, from data reported by Wei et al. [33] and Daw et al. [34]. At any given location in the powder domain, once melting occurs, the thermal conductivity curve is switched to that of solid IN625 (which is defined to melting temperature), since the particular location becomes part of the solid domain upon cooling. The initial condition for each powder layer L being spread is given by Eq. (4).

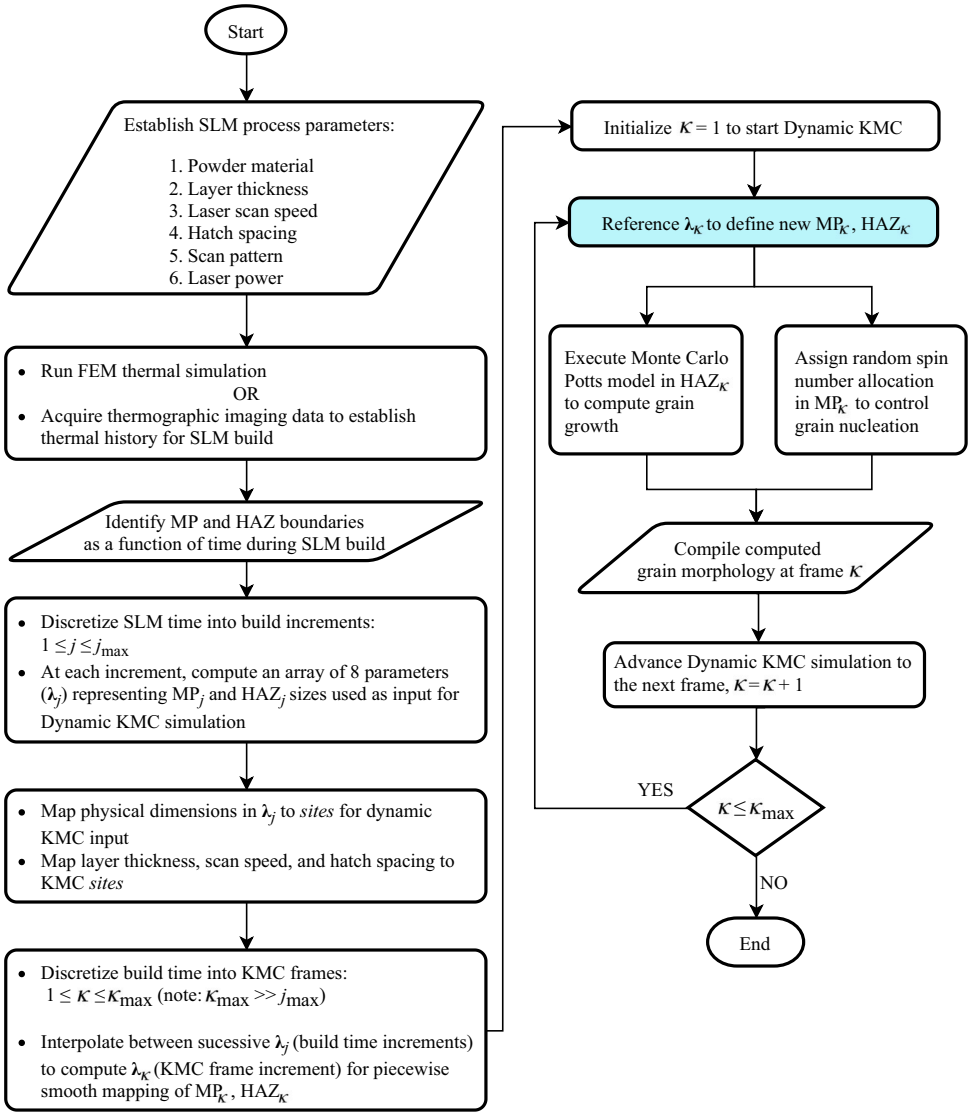

Fig. 3. An overview of the proposed Dynamic KMC framework. The key distinguishing step of the algorithm, illustrated by the shaded box, updates the MP and HAZ dimensions with every increment of time.

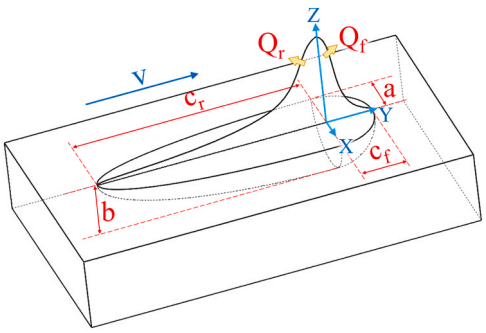

Fig. 4. Double ellipsoid heat source model [20].

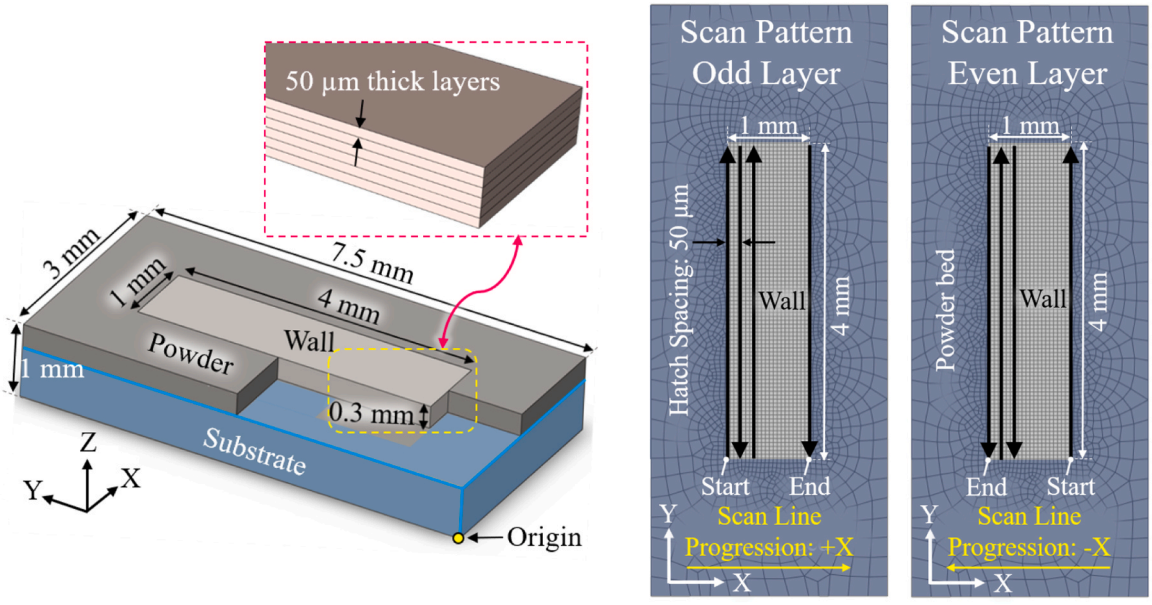

(a) **(b)**

Fig. 5. (a) Schematic of the SLM thin-walled structure and powder bed. (b) Bi-directional scan pattern, similar to [4].

$$T\left(t_{0,L}\right) = T_{\infty} \tag{4}$$

where T_{∞} is set as the ambient (or sink) temperature inside the printer (assumed 23 °C or 296.15 K).

Heat transfer and losses in the powder and solid continua are associated to internal conduction, as well as convection and radiation through the substrate and on free surfaces Γ of the active elements, respectively. The surface energy balance, described by Eq. (5), is recalculated at every time increment during the thermal simulation, [37].

$$\mathrm{k}\nabla T \cdot \hat{\boldsymbol{n}} = h(T - T_{\infty}) + \sigma\epsilon\left(T^4 - T_{\infty}^4\right) \quad \text{on free surfaces } \Gamma \tag{5}$$

where, h (W m^{-2} K^{-1}) is the convective heat transfer coefficient, σ is the Stefan–Boltzmann constant (5.6703 × 10^{-8} W m^{-2} K^{-4}), ϵ denotes the emissivity, and $\hat{\boldsymbol{n}}$ is the unit normal vector.

The powder layer deposition is modeled using the inactive elements approach [38,39]. Linear hexahedral diffusive heat transfer elements (DC3D8) having only a temperature degree of freedom are used. To reduce computational expense the substrate and powder surrounding the build is modeled using a relatively coarse swept mesh, whereas a relatively fine, structured, cubic element mesh is used to model the powder scanned to give the printed part. Mesh size (50 µm) corresponds to the powder layer thickness. The thermal solution is computed using the implicit solver of Abaqus v6.14, with a -IJDFLUX-İ user-subroutine coded in FORTRAN controlling the volumetric heat source, discussed next in Section 3.2.

3.2. Laser-induced heat source model

Popularly cited in literature, Goldak et al.'s double ellipsoid Gaussian heat source model (1984) [20], defined by Eq. (6), describes spatial and temporal thermal flux distribution, as induced by the laser in PBF-LB.

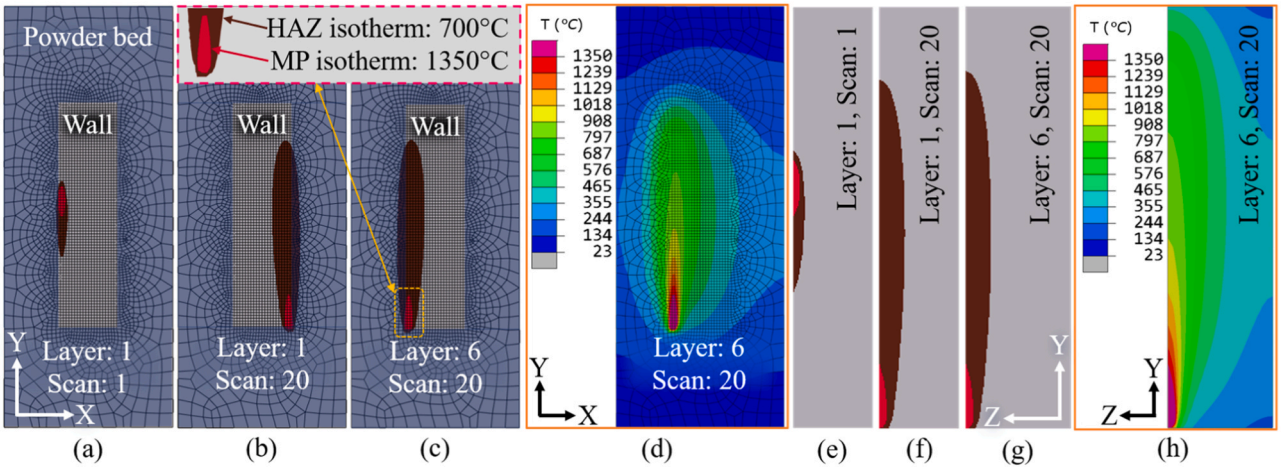

Fig. 6. Heat accumulation pattern on layers 1 and 6 at scans 1 and 20 when viewing (a - c) MP and HAZ isotherms from the top, (d) all isotherms from the top, (e - g) MP and HAZ isotherms through the depth, (h) all isotherms through the depth. Note, (a and e) represent a frame captured in the middle of scan 1 for layer 1, (b and f) represent a frame captured at the end of scan 20 for layer 1, and (c, d, g, and h) represent a frame captured at the end of scan 20 for layer 6.

$$Q = \begin{cases} \dfrac{6\sqrt{3}f_f P\alpha}{abc_f\pi\sqrt{\pi}} e^{-3\frac{x^2}{a^2}} e^{-3\frac{z^2}{b^2}} e^{-3\frac{(y+vt)^2}{c_f^2}}, & \forall \quad y \geq y_i \quad \text{for} \quad t > 0 \\ \dfrac{6\sqrt{3}f_r P\alpha}{abc_r\pi\sqrt{\pi}} e^{-3\frac{x^2}{a^2}} e^{-3\frac{z^2}{b^2}} e^{-3\frac{(y+vt)^2}{c_r^2}}, & \forall \quad y < y_i \quad \text{for} \quad t > 0 \end{cases} \tag{6}$$

In Eq. (6), Q (W m^{-3}) is the volumetric heat flux, P (W) is the laser power input, y_i is the instantaneous Lagrangian Y ordinate (assuming the scan proceeds in the Y direction), f_f and f_r are ratios of the heat distribution in the front and rear quadrants of the laser epicenter. Determining absorption efficiency (or absorptivity), α, of the powder particles, which may vary depending on mean particle size and size distribution, is discussed in Section 3.3. Remaining parameters used in Eq. (6) are specified in Table 1. Goldak et al.'s model is depicted in Fig. 4 where the volumetric heat source (or flux) Q assumes the shape of a single tailed comet, moving at scan speed v, and containing heat flux portions Q_f and Q_r distributed amongst the head and tail portions, respectively.

Eq. (6) controls the motion of the moving volumetric heat source with respect to start location, scan velocity, and time duration of individual linear scan paths. The heat flux is computed on every active integration point at every increment of time.

3.3. Thermal calibration

To calibrate unknown thermal model parameters such as absorptivity α, emissivity ϵ, and convective heat transfer coefficient h, which differ across various sources of literature [40–43], a physics-based FE simulation is created to replicate PBF-LB thermographic observations available from NIST [44], wherein a single IN625 powder layer was scanned over the substrate. Details of the IR thermography experiments can be found over a series of publications [31,45–48]. From the experimental data (and calibrated physics-based model), it is clear that the size and shape of the MP and HAZ vary within the single layer. Due to a dwell time of several seconds between successive layers in typical SLM operations, however, the variations in MP and HAZ are less dependent on build height. The corresponding calibrated values for α, ϵ, and h for Inconel 625 are listed in Table 2:

3.4. Heat transfer simulation for SLM build

Using the calibrated parameters in Table 2 for the described heat transfer model, a simulated 4 mm long × 1 mm wide × 0.3 mm tall thin-walled structure featuring six layers (each 50 μm thick) is built, as illustrated in Fig. 5a. Process parameters for the SLM build with Inconel 625 are adopted from the work of Wang et al. [49], as listed in Table 3. A hatch spacing of 50 μm is applied based on an SEM image in Li et al.'s work wherein the larger diameters of the Inconel 625 powder particles are reported to be approximately 45 μm [50]. The bi-directional scan

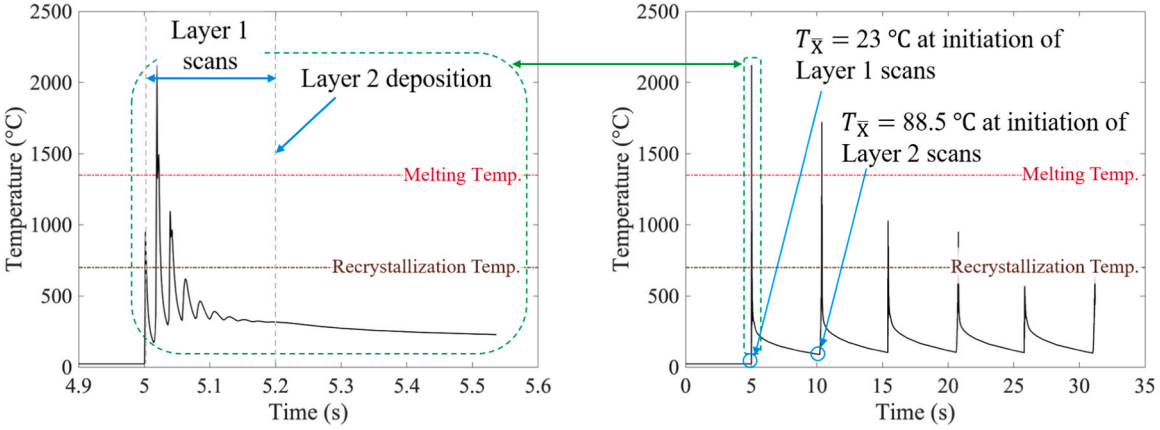

Fig. 7. *(Left)* Thermal history at an arbitrary point, $\bar{X}$ = (1.1, 2.15, 0.75) mm, in layer 1. *(Right)* Thermal history for the entire build probed at the same point.

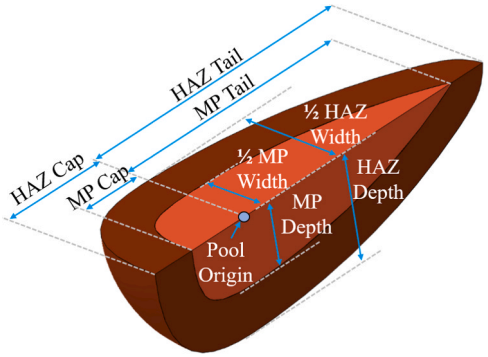

Fig. 8. Geometry control parameters for MP and HAZ.

pattern for the 6-layer build is depicted in Fig. 5b. Note that not all of the scan lines are shown. The pattern is selected based on work by [4].

While the Dynamic KMC framework considers both intralayer and interlayer heat accumulation, making it a versatile tool, suitable for microstructure prediction in both PBF and DED processes, upon execution of the SLM heat transfer model, there is clear evidence of intralayer heat accumulation, as seen in Fig. 6. Fig. 6a to 6c illustrate the growing MP and HAZ sizes when observed from above, i.e. viewed normal to the XY plane, while Figs. 6e to 6g provide the depth perspective, i.e. normal to the YZ plane. The predicted MP and HAZ appear to change considerably in size during the scans of a given layer, however the effect is less prominent across multiple build layers. Comparing Figs. 6a and 6b, there is obvious growth in the size of the MP and HAZ when progressing, respectively, from scan 1 to scan 20 within the same layer. Comparing Figs. 6b (layer 1) and 6c (layer 6), however, note that there is relatively little variation between the respective size of the MP and HAZ. The underlying reason is that the SLM process involves a multi-second dwell time during which the recoater blade spreads (deposits) a new layer of powder atop the last scanned layer. In the demonstrated FE model, a 5-second dwell time for recoating between successive layers is applied, as estimated from observations on an EOS M 290 printer [51]. Thus, even though some residual heat may transfer from the last scanned layer to the newly deposited powder layer, based on the predictions in Fig. 6, this interlayer heat accumulation in the SLM process is insignificant compared to the intralayer heat accumulation. A comparison of the growth in MP and HAZ is reported and discussed in more detail in Section 4. Note that Figs. 6a to 6c and Figs. 6e to 6g group isotherms above 700 °C, (HAZ boundary) and 1350 °C, (MP boundary), respectively, so the heat accumulation pattern is not as obvious. Fig. 6d and 6h, which display all the isotherms above ambient temperature, are therefore also included. In Fig. 6d, temperature distribution for the 20th (last) scan of the sixth layer is shown. An asymmetric intralayer heat accumulation pattern is clearly evident, and is the reason why the HAZs seen in Figs. 6b and 6c are also asymmetric. In addition, some intralayer heat accumulation perpendicularly ahead in terms of the scan line progression (i.e., in the -X direction relative to the MP) is also observed.

Table 1
Double ellipsoid heat source model parameters.

Parameter	Value
c_f	276 μm
c_r	1520 μm
a	160 μm
b	160 μm
f_f	1.4
f_r	0.6

Table 2
Calibrated thermal parameters used for SLM simulation with Inconel 625.

Powder absorptivity, α	Fused continua emissivity, ϵ	Convective heat transfer coefficient, h
0.67	0.67	10 W m^{-2} K^{-1}

Table 3
SLM process parameters to fabricate the thin-walled structure, [4,49].

Power	Scan speed	Scan pattern	Hatch spacing	Layer thickness
360 W	0.4 m s^{-1}	Bi-directional	50 μm	50 μm

Naturally, the intralayer heat accumulation during scans of a particular layer is a function of scan pattern, scan speed, laser power, powder properties, and part geometry. Temperature variation observed over a period of time can accordingly reflect the rapid thermal cycles during the build. This is clearly observed from Fig. 7 (Left) which shows the transient thermal history of an arbitrary point, $\overline{X} = (1.1, 2.15, 0.75)$ mm, located on the surface of the first layer being scanned. Note that very large temperature gradients are observed when the laser is in close proximity (or coincident) with the arbitrary point considered.

As subsequent layers are deposited, residual heat from previously scanned layers can accumulate to a limited degree. Fig. 7 (Right) shows the temperature for the same arbitrary point over the duration of the entire SLM build. The initial temperature of this point at the beginning of the second layer's scans is 88. 5 °C, whereas that for the first layer is only 23 °C, despite the SLM process parameters being unchanged. Again, very large temperature gradients are observed as the laser moves into close proximity with the point. This also affects the thermal history through the depth of the build. Grain growth and nucleation within a particular layer is thus still possible even during scans of subsequent layers since the MP and HAZ of layers above may still significantly influence the temperature of previously scanned layers. This circumstance, and its considerable effect on grain morphology, is clearly illustrated using the Dynamic KMC model, as discussed next.

4. Results and discussion on grain structure prediction using the Dynamic KMC model

Before discussing the grain structure variations that result in the SLM build according to the aforementioned thermal model results, it is important to note that Rodgers et al. [19] describes KMC not as an exhaustive and accurate grain structure prediction method but as an approximation tool that can provide grain size to input parameter

relationship. Accordingly, the grain structure obtained can vary depending on how the simulation is set up in terms of the simulated domain, laser scan parameters, and MP and HAZ sizing parameters. As depicted earlier in Fig. 3, the model bitmaps a continuum microstructure onto a lattice consisting of -IJsites-İ [7]. Simulation parameters are thus quantified in terms of sites, and therefore a mapping (or scaling) relationship between the physical dimensions and discrete KMC sites has to be ascertained to justify the size of the numerically predicted grain structures. In this study such prerequisite mapping calibration has been performed by comparing the KMC simulated results to those obtained through EBSD imaging [1,5]. The corresponding Dynamic KMC sites allocation for simulations that consider time-varying dimensions of the MP and HAZ parameters illustrated in Fig. 8, and which change in direct relation to the computed thermal history, are provided in Table 4. Note that the domain described in Table 4 considers a small cubic subregion rather than the entire thin-walled SLM structure, as discussed next.

Table 4
Dimensions for Dynamic KMC model parameters.

	Dimensions (min. - max.)
Domain	500 × 500 × 500 sites
MP Width	85–225 sites
MP Tail	420–1160 sites
MP Depth	85–100 sites
MP Cap	170–340 sites
HAZ Width	170–340 sites
HAZ Tail	1540–4316 sites
HAZ Depth	170–340 sites
HAZ Cap	170–425 sites
Scan speed	9 sites/time step
Hatch spacing	83 sites
Layer thickness	83 sites

Due to the lengthy computational time to perform KMC simulations for the entire build volume, grain structures for smaller volumetric subregions (0.3 mm × 0.3 mm × 0.3 mm) at different locations of the 3D-simulated AM build are compared. As shown in Fig. 9, each SLM layer of the wall is divided into 4 regions (1 mm × 1 mm each). Of these four 1 mm^2 regions, those denoted 1 and 4 have three surfaces interfacing with the surrounding powder bed, whereas regions denoted 2 and 3 have only two. For this reason, relatively greater intralayer heat accumulation occurs in regions 2 and 3 than in regions 1 and 4. This is because the laser scan lines always commence and terminate in regions 1 and 4, resulting in less intralayer heat accumulation compared to regions 2 and 3.

This particular discussion reveals a challenge and limitation of the KMC model since the moving heat source effectively "turns around" near the edges of the build, which subsequently leads to profiles of the MP and HAZ that cannot be represented using only the eight parameters illustrated in Fig. 8. In this work, such behavior of the MP and HAZ near the edges of the build is referred to as *edge effects*, and is not addressed in this particular study since the predicted grain structures discussed herein apply to the smaller 0.3 mm × 0.3 mm enumerated planar subregions in Fig. 9, which are located away from the extreme edges of the SLM build. Predicted grain structures in these smaller, planar subregions are examined at various layers following completion of the entire 6-layer build process, in which each layer is 50 μm thick.

Considering results of layer 1, seen in Fig. 9 (Left), it is clear that subregion 1 has visibly smaller grains compared to subregion 3. Individual grain shapes within the planar subregions 1 and 3 are elliptically fit with major and minor diameters ($\varnothing_{Major}$ and $\varnothing_{Minor}$), for which the distribution fraction for $\varnothing_{Major}$ is quantified in Fig. 9 (Right). Note that the major diameter of the non-equiaxed grains corresponds to the lowest

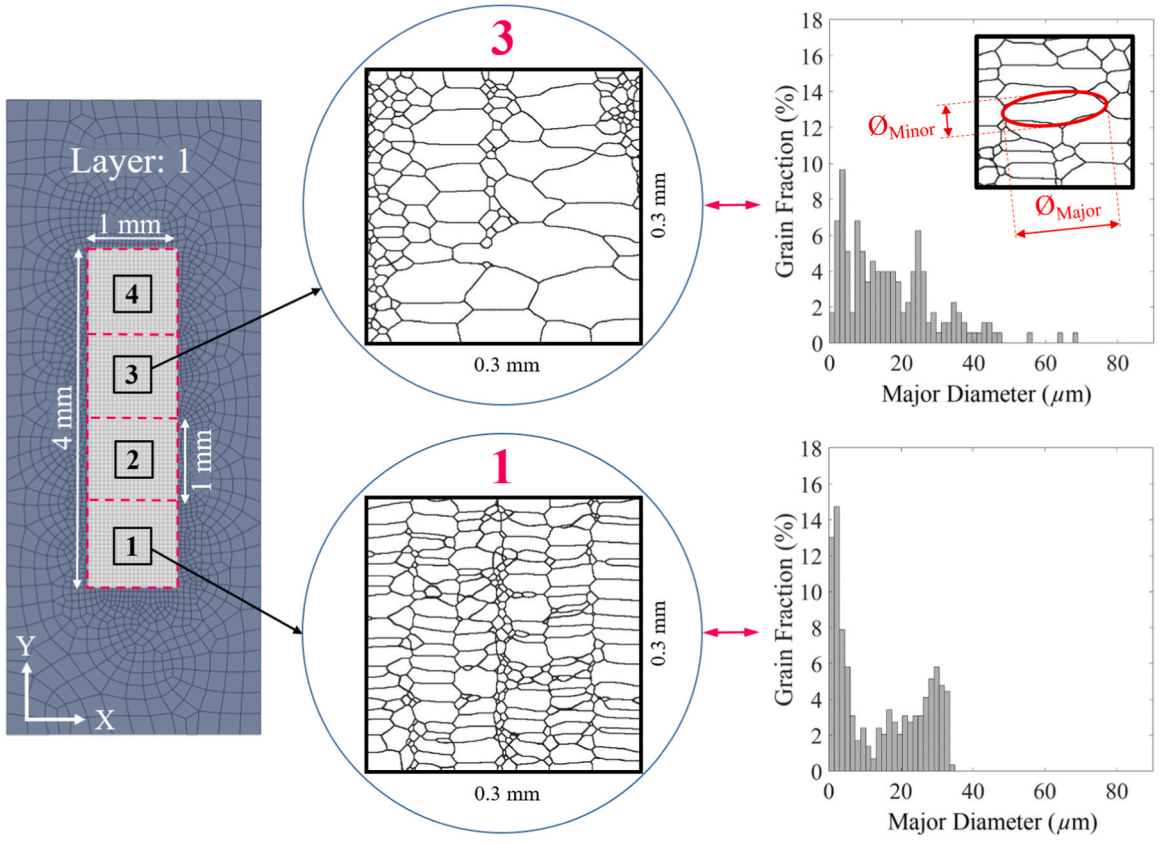

Fig. 9. (*Left*) Planar view of the 3D grain structure prediction for subregions 1 and 3 in layer 1. (*Right*) Histograms depicting the distribution fraction of grains in respective subregions based on major diameter.

strength direction of the polycrystalline alloy, per the Hall–Petch relationship [4,52–55], and is hence treated as the metric with which to compare grain size distributions. Fig. 9 (Right) offers a quantitative perspective of grain size distribution across both subregions 1 and 3. The reasons for grain morphology differences between subregions 1 and 3 are better understood when comparing the MP and HAZ dimensions within those subregions during scans of layer 1, as observed in Fig. 10. In addition, a quantitative perspective of the maximum MP and HAZ dimensions for subregions 1 and 3 in all six layers of the AM build is reported in Table 5.

From Table 5 two preliminary observations are made. Firstly, all the HAZ dimensions (length, width, and depth) observed in subregion 3, for the six printed layers, are greater than those for subregion 1. The MP dimensions reveal the opposite trend, with nearly all the dimensions for subregion 1 exceeding those observed for subregion 3. Given that nucleation is controlled by the occurrence of the MP, and grain growth in facilitated by the occurrence of the HAZ, the aforementioned trends offer a clear explanation for the grain structures predicted in Figs. 9 and 11 to 13. Secondly, the HAZ dimensions for both subregions across all six layers appear to increase up to layer 3 or 4 and then drop. This pattern reveals how the HAZ is influenced by interlayer heat transfer. As the first few layers build, heat accumulates because there is insufficient heat transferred away by conduction (through solid continua). As the build progresses with more solid continua being added, the amount of thermal conduction increases. Heat is carried away at a faster rate, thereby limiting the amount that can accumulate, and thus limiting the growth of the HAZ.

While all the scans move in the ± Y direction, the scan lines of layer 1 progress in the + X direction, as seen in Fig. 5b. Heat thus accumulates towards the right, i.e. + X direction. Contrary to this, the grains in subregion 3 appear to get larger progressing toward the left. As mentioned earlier, however, the final shape of grains in a layer is influenced not only by the scans within that layer, but also the scans of subsequent layers since their heat fluxes also influence lower layers.

Considering layer 2, wherein scan lines progress in the -X direction, it is clearly seen in Fig. 11a that the MP and HAZ penetrate down to layer 1, and thus influence grain nucleation and growth in layer 1. When observing grain structures for subregions 1 and 3 in layer 2, seen in Fig. 11c, it is clear that subregion 1 has smaller grains overall compared to subregion 3. Referring to the MP dimensions of layer 2 in Table 5, the size of the MP is larger for subregion 1 relative to subregion 3, which drives greater nucleation, hence explaining the increased number of smaller grains visible in subregion 1 as compared to subregion 3.

Referring back to the EBSD images documented by Fang et al. [1], as seen in Fig. 1d, grain structures at different locations along the build height direction (Z-axis) are seen to vary. Note there is a relative elongation in the grains, which appear to align towards the direction of maximum thermal gradient. Thus, when a cross section (XY plane) is imaged, one needs to be cognizant of the fact that some of these elongated grains may appear as equiaxed, which may be contrary to the actual 3D morphology. The same 2D imaging limitation is simulated when viewing planar grain structures using the Dynamic KMC framework, making it challenging to observe any obvious trends in layer 2, progressing in the +X or -X direction. While the scan lines for layer 2 progress in the -X direction, the scan lines for layer 3 progress in the +X direction, and the scans for layer 4, whose HAZ penetrates down to layer 1 as seen in Fig. 11b, progress in the -X direction as well. Such is also the case for layer 3; in comparison to layer 1, it is observed that the grains predicted are relatively larger in layer 3. Judging by grain size distribution in Fig. 12 (Right), in subregion 1 of layer 3 there is a comparatively lower fraction (~ 9%) of finer grains ($\varnothing_{Major}$ ~ 0–5 μm), relative to the same subregion observed in layer 1 (~ 15%). The size difference

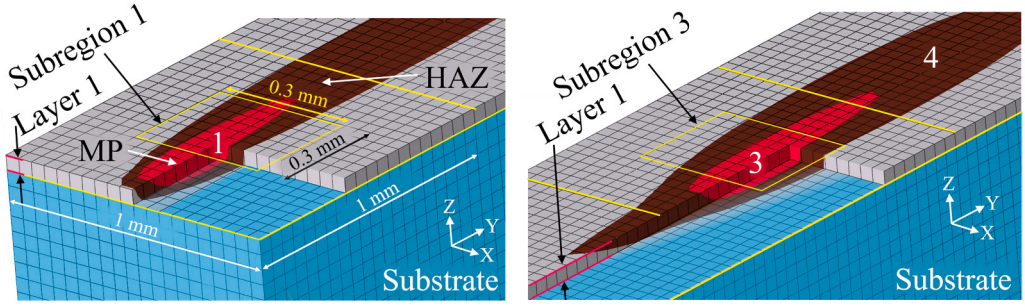

(a) (b)

Fig. 10. Comparison of MP and HAZ between (a) subregion 1 and (b) subregion 3 in layer 1.

Table 5
Maximum MP and HAZ dimensions computed by the FE model at the center of subregions 1 and 3 in all six layers.

Subregion	Layer	Melt Pool, MP			Heat Affected Zone, HAZ		
		Length (μm)	Width (μm)	Depth (μm)	Length (μm)	Width (μm)	Depth (μm)
1	1	850	160	90	1900	400	190
	2	850	160	90	2025	400	200
	3	870	175	90	2275	425	200
	4	865	175	90	2275	420	200
	5	880	175	95	2225	420	200
	6	900	175	80	2225	400	195
3	1	800	150	75	3000	450	215
	2	825	145	75	3050	450	225
	3	850	150	80	3135	475	250
	4	855	145	80	3150	470	245
	5	900	150	75	3125	475	240
	6	825	150	80	3100	450	225

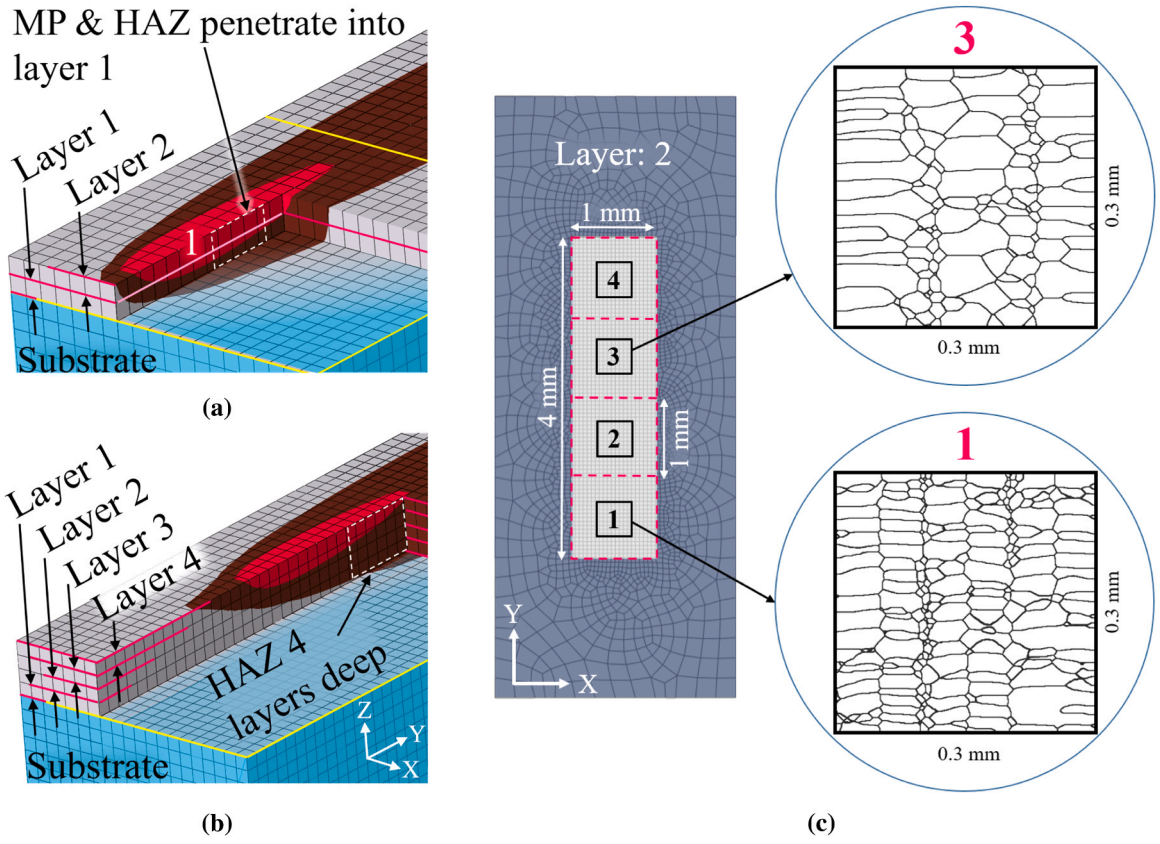

Fig. 11. (a) Layer 2 MP and HAZ penetration depth. (b) Layer 4 MP and HAZ penetration depth. (c) Planar view of the 3D grain structure prediction for layer 2.

when comparing subregion 3 in layer 1 and in layer 3 is visibly obvious (as seen in Figs. 9 and 12) and a quantitative comparison is not needed; the reason for such difference in grain size is the amount of heat accumulation in region 2 (and 3) of the printed structure. Layer 3 is not only affected by the interlayer heat accumulation from the previously printed layers but is also affected by the occurrence of MP and HAZ during scans of layers 4, 5, and 6, which are processed subsequently.

All the layers discussed thus far have at least three layers printed above them. To help understand the magnitude of influence of the MP and HAZ presence from fewer subsequently printed layers, the grain structures for layer 5 are examined. Layer 5 has only one subsequently printed layer (i.e. layer 6). From Fig. 13 (Left) the overall trend in grain structure is similar to those seen for layers 2 and 3, however an increased number of smaller grains appear, as quantified in Fig. 13 (Right). The small grains observed in layer 5 could be a direct result of augmented nucleation during the processing of layer 6. With only one layer printed above, the grains in layer 5 do not appear to grow further, as they do for layers 2, 3 and 4 (not shown).

EBSD imaging as seen in Fig. 1c, reported in the work of Sun et al. [5], concurs with the observed trend. An EBSD imaged microstructure cross section formed along the build direction is shown in Fig. 1c. Spherical as well as shorter columnar grains are seen towards the top of section D, in comparison to the grain structure observed in section C where a majority of the grains appear to be columnar and aligned to the direction of maximum thermal gradient.

To offer some perspective on the underlying hypothesis that heat accumulation leads to variation in the dimensions of MP and HAZ, which in turn leads to variation in grain structure, another KMC simulation is run in which the MP and HAZ dimensions do not vary with time and are thus held constant throughout the entire build process, i.e., implying steady-state conditions. Such is the practice described in the existing (modified) KMC [19,25,26,2,27,28].

In the case of steady-state MP and HAZ, it is not necessary to examine different subregions for the same layer. Fig. 14 reveals the grain structures predicted in layers 1, 2 and 3. Note that there is little to no observable change in grain size and shape across the different layers. Since the effects of heat accumulation are not captured, grain structures appear relatively consistent across the different layers, in contradiction to that which is observed with the Dynamic KMC model and in addition to what has been documented in works of [5,3,6].

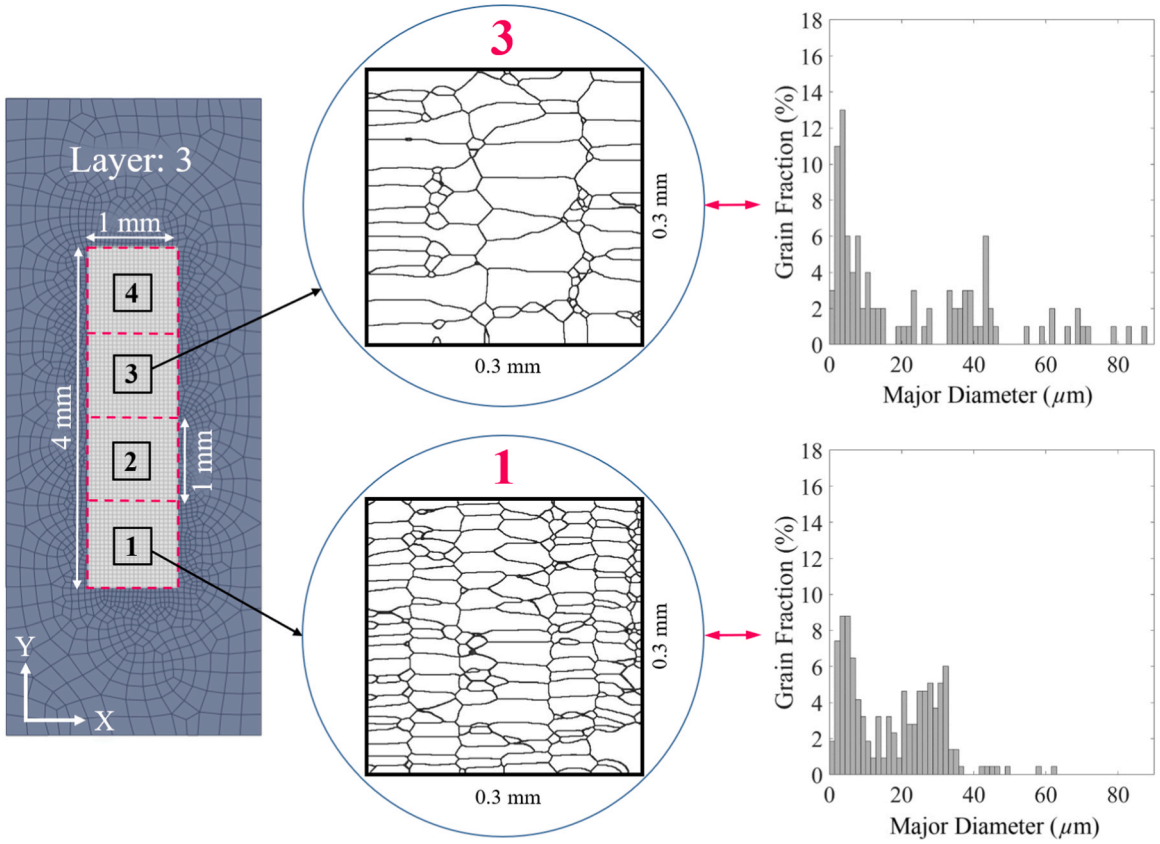

Fig. 12. (*Left*) Planar view of the 3D grain structure prediction for subregions 1 and 3 in layer 3. (*Right*) Histograms depicting the distribution fraction of grains in respective subregions based on major diameter.

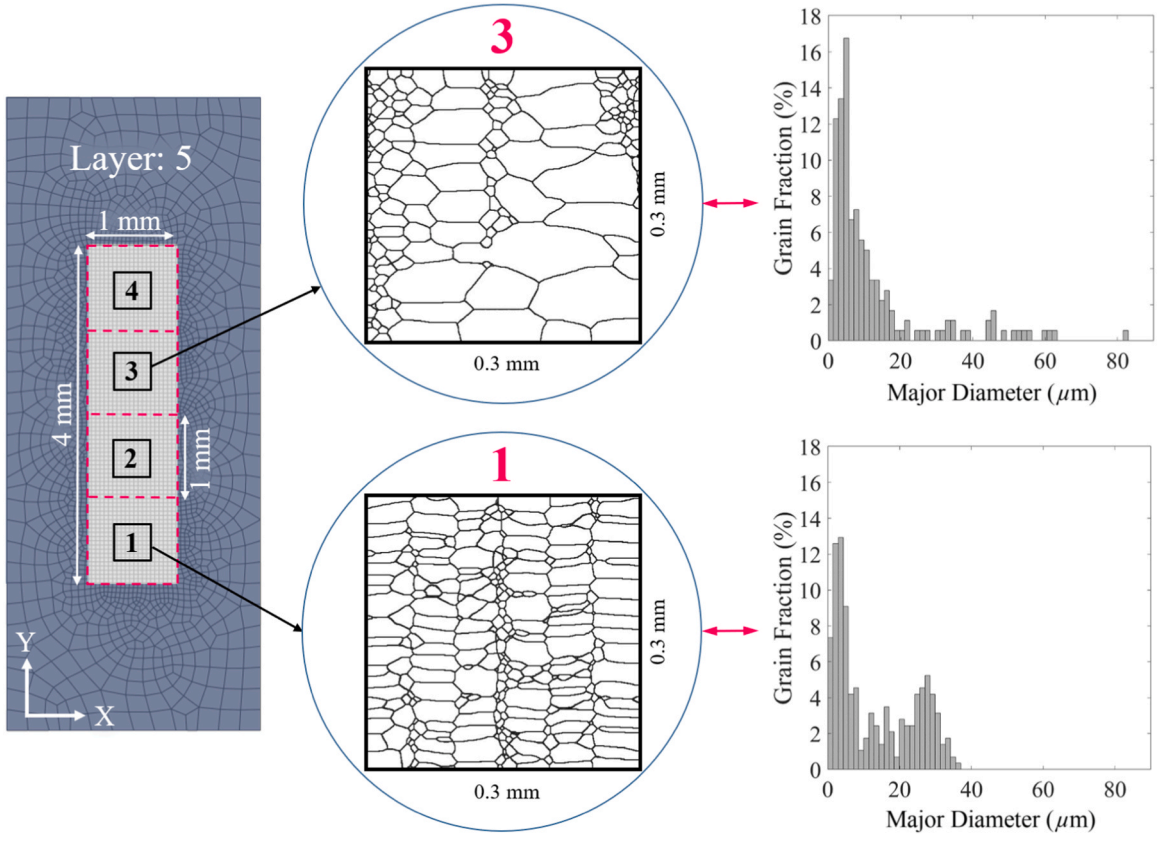

Fig. 13. (*Left*) Planar view of the 3D grain structure prediction for subregions 1 and 3 in layer 5. (*Right*) Histograms depicting the distribution fraction of grains in respective subregions based on major diameter.

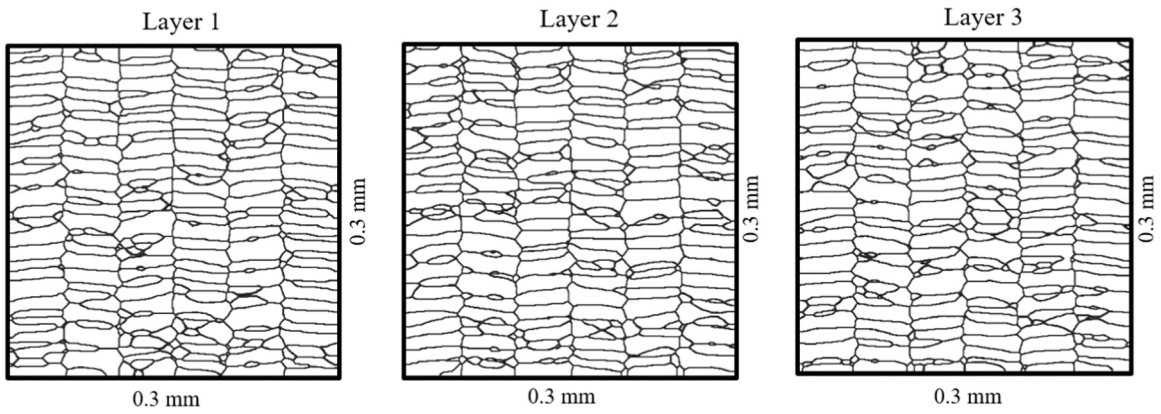

Fig. 14. Planar views of the 3D grain structure prediction when using the conventional KMC method. No variation in trend is observed across the different layers or different regions of the same layer.

5. Conclusion

A Dynamic KMC framework is proposed to predict grain structures for metal PBF and DED AM builds. While the existing KMC model in literature was validated with EBSD imaging, the particular validation was relevant only over a very limited region of the build [19], and did not consider the transient thermal history of the AM process. On contrary, the Dynamic KMC framework introduced and demonstrated in this work updates the MP and HAZ dimensions at every frame of time during the KMC simulation algorithm, thus capturing the dynamic behavior of the MP and HAZ as a result of heat accumulation over the duration of the build.

A thermal FE simulation of the SLM build process for an IN625 thin-walled structure is created. The FE model demonstrates temporal variation in dimensions of the MP and HAZ in different regions of the AM build, as influenced by intralayer heat accumulation. In-situ thermographic imaging of the PBF-LB process (with IN625) is used to calibrate the thermal simulation [31]. IR imaging data for the entire AM process, if available, can also be used with the Dynamic KMC algorithm in lieu of a calibrated thermal FE model.

The novel framework that couples non-uniform temperature distribution during the rapid SLM thermal cycles with the Dynamic KMC model is tested, and the resulting grain structures are compared to trends observed in literature. For the 6-layer thin-walled IN625 part studied, insights from the Dynamic KMC simulations reveal:

- Variations in grain structures amongst different regions within the same build layer, as well as between different build layers.
- Predicted grain structures in regions located centrally within a build layer differ from those located closer to the ends of the wall due to the differing number of powder interfaced surfaces, scan line terminations, and the corresponding differences in heat transfer rates.
- As a consequence of reduced intralayer heat accumulation, grains predicted to form near the ends of the thin AM wall are generally smaller than those formed in the central regions.
- The predicted HAZ of a particular layer is observed to drive the growth of grains that nucleate in underlying layers, according to their proximity, while the penetration of the MP into underlying layers is believed to cause re-melting and thus drive secondary nucleation in lower layers of the build.
- The grains predicted in the lower layers grow in the direction of maximum thermal gradient and can therefore penetrate into higher (newly deposited) layers. When examining the cross section of a layer, such effects may deceptively manifest in the form of equiaxed grains, even though such grains are elongated.
- An increased number of smaller grains may appear on an upper layer (near the solidification front) relative to lower layers, if there are not many subsequent layers printed above whose HAZ influences further grain growth (elongation). Similar observations and microstructural trends to those shown with the presented Dynamic KMC framework are reported in the EBSD studies of [4,5,1].

The presented Dynamic KMC framework can therefore offer a useful simulation tool for predicting more realistic grain morphology over differing regions of metal PBF and DED AM parts. Improved insights into the grain structure evolution can also better enable assessments into the non-homogeneity and anisotropic mechanical property behavior in AM parts according to the transient thermal history of the build process.

Declaration of Competing Interest

The authors declare that they have no known competing financial interests or personal relationships that could have appeared to influence the work reported in this paper.

Acknowledgment

The authors acknowledge the support of U.S. National Science Foundation, grant no. CMMI-1762722. Any opinions, findings, or conclusions expressed in this paper are those of the authors and do not necessarily reflect the views of the U.S. National Science Foundation.

References

[1] X. Fang, H. Li, M. Wang, C. Li, Y. Guo, Characterization of texture and grain boundary character distributions of selective laser melted inconel 625 alloy, Mater. Charact. 143 (2018) 182–190.
[2] W. Li, M. Soshi, Modeling analysis of the effect of laser transverse speed on grain morphology during directed energy deposition process, Int. J. Adv. Manuf. Technol. 103 (9–12) (2019) 1–13.
[3] L.N. Carter, C. Martin, P.J. Withers, M.M. Attallah, The influence of the laser scan strategy on grain structure and cracking behaviour in slm powder-bed fabricated nickel superalloy, J. Alloy. Compd. 615 (2014) 338–347.
[4] Z. Wang, T.A. Palmer, A.M. Beese, Effect of processing parameters on microstructure and tensile properties of austenitic stainless steel 304l made by directed energy deposition additive manufacturing, Acta Mater. 110 (2016) 226–235.
[5] D. Sun, X. Li, W. Tan, A parametric study on grain structure in selective laser melting process for stainless steel 316l, in: Proceedings of the 28th Annual International Solid Freeform Fabrication Symposium-An Additive Manufacturing Conference, Austin, TX, USA, 2017, pp.7–9.
[6] S. Holland, X. Wang, J. Chen, W. Cai, F. Yan, L. Li, Multiscale characterization of microstructures and mechanical properties of inconel 718 fabricated by selective laser melting, J. Alloy. Compd. 784 (2019) 182–194.
[7] E.A. Holm, C.C. Battaile, The computer simulation of microstructural evolution, JOM 53 (2001) 20–23.
[8] Y. Liu, T. Baudin, R. Penelle, Simulation of normal grain growth by cellular automata, Scr. Mater. 34 (1996).
[9] J. Zhang, F. Liou, W. Seufzer, J. Newkirk, Z. Fan, H. Liu, T.E. Sparks, Probabilistic simulation of solidification microstructure evolution during laser-based metal

deposition, in: Proceedings of 2013 Annual International Solid Freeform Fabrication Symposium-An Additive Manufacturing Conference, (2013).
[10] D.S. Svyetlichnyy, Modeling of grain refinement by cellular automata, Comput. Mater. Sci. 77 (2013) 408–416.
[11] A. Zinoviev, O. Zinovieva, V. Ploshikhin, V. Romanova, R. Balokhonov, Evolution of grain structure during laser additive manufacturing. simulation by a cellular automata method, Mater. Des. 106 (2016) 321–329.
[12] Y. Lian, S. Lin, W. Yan, W.K. Liu, G.J. Wagner, A parallelized three-dimensional cellular automaton model for grain growth during additive manufacturing, Comput. Mech. 61 (5) (2018) 543–558.
[13] A.A. Antonysamy, J. Meyer, P. Prangnell, Effect of build geometry on the β -grain structure and texture in additive manufacture of ti6al4v by selective electron beam melting, Mater. Charact. 84 (2013) 153–168.
[14] Y. Ji, L. Chen, L.-Q. Chen, Understanding microstructure evolution during additive manufacturing of metallic alloys using phase-field modeling, in: Thermo-Mechanical Modeling of Additive Manufacturing, Elsevier, 2018, pp. 93–116.
[15] A. Antonysamy, Mechanical Property Evolution During Additive Manufacture of Ti6al4v Alloy Using Laser, Electron Beam, and Arc Melting Techniques for Aerospace Applications, University of Manchester, 2012. PhD Thesis.
[16] R.B. Potts, Some generalized order-disorder transformations, in: Mathematical Proceedings of the Cambridge Philosophical Society, Cambridge University Press, 1952, pp. 106–109.
[17] M. Anderson, D. Srolovitz, G. Grest, P. Sahni, Computer simulation of grain growth-i. kinetics, Acta Metall. 32 (5) (1984) 783–791.
[18] L.L. Parimi, G. Ravi, D. Clark, M.M. Attallah, Microstructural and texture development in direct laser fabricated in718, Mater. Charact. 89 (2014) 102–111.
[19] T.M. Rodgers, J.D. Madison, V. Tikare, Simulation of metal additive manufacturing microstructures using kinetic monte carlo, Comput. Mater. Sci. 135 (2017) 78–89.
[20] J. Goldak, A. Chakravarti, M. Bibby, A new finite element model for welding heat sources, Metall. Trans. B 15 (2) (1984) 299–305.
[21] W. Huang, Y. Zhang, Finite element simulation of thermal behavior in single-track multiple-layers thin wall without-support during selective laser melting, J. Manuf. Process. 42 (2019) 139–148.
[22] N. Hodge, R. Ferencz, J. Solberg, Implementation of a thermomechanical model for the simulation of selective laser melting, Comput. Mech. 54 (1) (2014) 33–51.
[23] S. Shrestha, T. Starr, K. Chou, Porosity analysis in metal additive manufacturing by micro-ct, in: ASME 2018 International Mechanical Engineering Congress and Exposition, American Society of Mechanical Engineers Digital Collection, 2018.
[24] S. Shrestha, T. Starr, K. Chou, A study of keyhole porosity in selective laser melting: single-track scanning with micro-ct analysis, J. Manuf. Sci. Eng. 141 (2019).
[25] W. Yan, S. Lin, O.L. Kafka, Y. Lian, C. Yu, Z. Liu, J. Yan, S. Wolff, H. Wu, E. Ndip-Agbor, et al., Data-driven multi-scale multi-physics models to derive process-structure-property relationships for additive manufacturing, Comput. Mech. 61 (5) (2018) 521–541.
[26] W. Yan, S. Lin, O.L. Kafka, C. Yu, Z. Liu, Y. Lian, S. Wolff, J. Cao, G.J. Wagner, W. K. Liu, Modeling process-structure-property relationships for additive manufacturing, Front. Mech. Eng. 13 (4) (2018) 482–492.
[27] T.M. Rodgers, J.E. Bishop, J.D. Madison, Direct numerical simulation of mechanical response in synthetic additively manufactured microstructures, Model. Simul. Mater. Sci. Eng. 26 (5) (2018), 055010.
[28] T.M. Rodgers, H. Lim, J.A. Brown, Three-dimensional additively manufactured microstructures and their mechanical properties, JOM 72 (2020) 75–82.
[29] S. Geneva, Additive Manufacturing—General Principles—Terminology, ISO/ASTM, 2015, 52900.
[30] H. Wei, G. Knapp, T. Mukherjee, T. DebRoy, Three-dimensional grain growth during multi-layer printing of a nickel-based alloy inconel 718, Addit. Manuf. 25 (2019) 448–459.
[31] J.C. Heigel, B.M. Lane, Measurement of the melt pool length during single scan tracks in a commercial laser powder bed fusion process, J. Manuf. Sci. Eng. 140 (2018), 051012.
[32] M. Gouge, P. Michaleris, Thermo-mechanical Modeling of Additive Manufacturing, Butterworth-Heinemann, 2017.
[33] L.C. Wei, L.E. Ehrlich, M.J. Powell-Palm, C. Montgomery, J. Beuth, J.A. Malen, Thermal conductivity of metal powders for powder bed additive manufacturing, Addit. Manuf. 21 (2018) 201–208.
[34] J. Daw, J. Rempe, D. Knudson, Thermal Properties of Structural Materials Found in Light Water Reactor Vessels, Idaho National Laboratory (INL), 2009. Technical Report.
[35] Z. Wang, E. Denlinger, P. Michaleris, A.D. Stoica, D. Ma, A.M. Beese, Residual stress mapping in inconel 625 fabricated through additive manufacturing: method for neutron diffraction measurements to validate thermomechanical model predictions, Mater. Des. 113 (2017) 169–177.
[36] A. Foroozmehr, M. Badrossamay, E. Foroozmehr, S. Golabi, Finite element simulation of selective laser melting process considering optical penetration depth of laser in powder bed, Mater. Des. 89 (2016) 255–263.
[37] D.W. Hahn, M.N. Özisik, Heat Conduction, John Wiley & Sons, 2012.
[38] P. Michaleris, Modeling metal deposition in heat transfer analyses of additive manufacturing processes, Finite Elem. Anal. Des. 86 (2014) 51–60.
[39] L.-E. Lindgren, H. Runnemalm, M.O. Näsström, Simulation of multipass welding of a thick plate, Int. J. Numer. Methods Eng. 44 (9) (1999) 1301–1316.
[40] P. Kieruj, D. Przestacki, T. Chwalczuk, Determination of emissivity coefficient of heat-resistant super alloys and cemented carbide, Arch. Mech. Technol. Mater. 36 (1) (2016) 30–34.
[41] C. Boley, S. Mitchell, A. Rubenchik, S. Wu, Metal powder absorptivity: modeling and experiment, Appl. Opt. 55 (23) (2016) 6496–6500.
[42] C. Montgomery, J. Beuth, L. Sheridan, N. Klingbeil, Process mapping of inconel 625 in laser powder bed additive manufacturing, in: Solid freeform fabrication symposium, 2015, pp.1195–1204.
[43] M. Masoomi, A. Soltani-Tehrani, N. Shamsaei, S.M. Thompson, Convection heat transfer coefficients for laser powder bed fusion, 2018.
[44] NIST LPBF Thermographic Observations, ⟨https://www.NIST.gov/el/lpbf-thermography/datasets/single-layers-and-tracks⟩, 2017. (Accessed 27 March 2020).
[45] S. Moylan, E. Whitenton, B. Lane, J. Slotwinski, Infrared thermography for laser-based powder bed fusion additive manufacturing processes, in: AIP Conference Proceedings, 1581, AIP, 2014, pp.1191–1196.
[46] B. Lane, E. Whitenton, S. Moylan, Multiple sensor detection of process phenomena in laser powder bed fusion, in: Thermosense: Thermal Infrared Applications XXXVIII, 9861, International Society for Optics and Photonics, 2016.
[47] J.C. Heigel, B.M. Lane, The effect of powder on cooling rate and melt pool length measurements using in situ thermographic techniques, in: Solid freeform fabrication symposium, 2017.
[48] B. Lane, S. Moylan, E.P. Whitenton, L. Ma, Thermographic measurements of the commercial laser powder bed fusion process at nist, Rapid Prototyp. J. 22 (5) (2016) 778–787.
[49] P. Wang, B. Zhang, C.C. Tan, S. Raghavan, Y.-F. Lim, C.-N. Sun, J. Wei, D. Chi, Microstructural characteristics and mechanical properties of carbon nanotube reinforced inconel 625 parts fabricated by selective laser melting, Mater. Des. 112 (2016) 290–299.
[50] C. Li, R. White, X. Fang, M. Weaver, Y. Guo, Microstructure evolution characteristics of inconel 625 alloy from selective laser melting to heat treatment, Mater. Sci. Eng. A 705 (2017) 20–31.
[51] M. Solutions The additive manufacturing system for the production of serial components, spare parts and functional prototypes directly in metal, EOS, 1000, 2014, 290.
[52] L.-E. Lindgren, A. Lundbäck, M. Fisk, R. Pederson, J. Andersson, Simulation of additive manufacturing using coupled constitutive and microstructure models, Addit. Manuf. 12 (2016) 144–158.
[53] Y. Gao, M. Zhou, Superior mechanical behavior and fretting wear resistance of 3d-printed inconel 625 superalloy, Appl. Sci. 8 (12) (2018), 2439.
[54] N. Petch, The cleavage strength of polycrystals, J. Iron Steel Inst. 174 (1953) 25–28.
[55] E. Hall, The deformation and ageing of mild steel: Iii discussion of results, Proc. Phys. Soc. Sect. B 64 (1951) 747.